Proceedings of the 21st ICSMGE, Vienna, Austria, 14 – 19 June 2026. Pistrol, Adam & Schweiger (eds.)
Published by: ÖGG, Austrian Society for Geomechanics, Salzburg, Austria, ISBN 978-3-9503898-4-5
https://doi.org/10.53243/ICSMGE2026-2287

Material Point Method modelling of offshore unburied cable/pipe interacting with soil

Mateu Maglia
Universitat Politècnica de Catalunya (UPC), Spain, mateu.maglia@upc.edu

Núria M.Pinyol
Universitat Politècnica de Catalunya (UPC), Spain
International Centre for Numerical Methods in Engineering (CIMNE), Spain

Christian Hoffman
VanOord, Rotterdam, The Netherlands

ABSTRACT: In a context of climate emergency decarbonization of energy is one of the main goals at the global level, and renewable energies are growing in share to substitute energy traditionally coming from hydrocarbons. The offshore environment has traditionally been used by oil and gas extraction industry, and now the accumulated knowledge in this field can be transferred to renewable energies such as offshore wind power plants. Both industries need to transport the energy onshore by pipelines or cables that are usually laid on soil surface relying only on soil bearing capacity to withstand installation and service loads. The assessment of soil reaction to embedment and lateral pipe movement is a key aspect to correctly install and dimension these structures. Material remolding and deformation in cable installation and service can play an important role in soil reaction as occurs in unburied pipe-soil interaction problems. For that reason, including large deformation analysis can have some benefits over classical bearing capacity solutions or standard finite element method (FEM) analysis. In this study, the material point method (MPM) implemented in the open-source code Anura3D, able to simulate large deformations and soil-water-structure interaction, is selected to study pipe/cable-soil interaction. The contact formulation, based on a velocity predictor-corrector scheme is addressed and improved. The numerical approach and its developments are validated against an instrumented centrifuge experiment in which a rigid pipe interacts with saturated sandy soil. The results compared with a current industry procedure known as the "wished-in-place" (WIP) method. This method is based on standard FEM analysis and cannot simulate large deformations or account for material remolding; instead, the deformed geometry is imposed directly. This work shows that MPM is a powerful tool to address problems where large deformation plays an important role.

KEYWORDS: Offshore, pipe-soil interaction, numerical modelling, large deformation, MPM, contact algorithm.

1 INTRODUCTION

Energy decarbonization is one of the main objectives at global scale to reduce global warming. The European Union emissions reduction target has increased from a 40% to a 55% in 2030 compared to 1990 levels (EC, 2020a). Renewable energies are growing in share to fulfil these objectives and they are expected to grow more in next decades. The installation of this energy facilities, such as wind or solar farms, inlands encounters some difficulties due to social rejection or lack of space. This makes necessary to consider the construction of new renewable energy facilities offshore. The main example would be offshore wind farms, which are expected to grow from an installed capacity of 57GW in 2023 to 2000GW in 2050, getting around 20% of the total onshore and offshore global wind energy capacity (EC, 2020b).

Offshore environment has been traditionally used for oil and gas industry, and the accumulated knowledge in the field can be transmitted to offshore renewable energy facilities. An example of a similar problem encountered in both hydrocarbons and renewable energy is the transport of energy, with pipes in the first case and cables in the second. In deep waters, both linear structures are usually laid on the bottom of the sea without any further structure, relying on surface soil bearing capacity to withstand installation and service loads. This includes a large number of different loads such as self-weight, installation procedures stress concentration, subsea currents, buckling due to thermal changes and cyclic wave action. This produces a complex stress life on bearing soil that includes large mobilization of seabed material and degradation of its properties. Because of that, vertical and horizontal movements are expected, and soil reaction is a key aspect to predict them (Dingle et al. 2008).

Classic bearing capacity solutions for pipelines (Murff et al. 1989) were developed for pure vertical embedment movements. Results tend to underpredict real cases information as vertical movements are greater than the ones supposed by self-weight because of horizontal and vertical cyclic loading and stress concentration during installation (Westgate et al. 2009). Initial embedment is an important aspect of the problem, because lateral resistance arises partially from passive pressure generated by mobilized material around the pipe (Gourvenec & Randolph, 2011).

Another available solution is given by yield envelopes combining vertical and horizontal displacements based on plasticity limit analysis for drained (Zhang et al. 2002) and undrained cases (Randolph & White 2008b). These solutions have been validated with geotechnical centrifuge test data (Dingle et al 2008, Wang et al. 2010).

Numerical modelling of the full embedment-lateral movement process needs large deformation methods capable of predicting material remolding. The great majority of cases in literature (Merifield et al. 2008, 2009; Wang et al. 2010; Chatterjee et al. 2012) are modelled with Remeshing and Interpolation Technique with Small Strain (RITSS) (Hu & Randolph 1998), which falls in the category of Arbitrary Lagrangian-Eulerian (ALE) methods (Ghosh & Kikuchi 1991).

This paper addresses the simulation of the embedment and lateral movement of an unburied pipeline–soil interaction using the material point method (MPM) (Sulsky et al., 1994). Particular emphasis is placed on the contact formulation required to model the interaction between rigid bodies and deformable soils. The open-source Anura3D code (Anura3D MPM Research Community, 2025) is employed, incorporating several developments aimed at improving contact detection accuracy and numerical stability.

The results are validated against centrifuge test data for calcareous sand reported in the literature (Zhang et al., 1999). Additionally, a small-strain FEM analysis is performed using

the "wished-in-place" (WIP) procedure to highlight the differences between the two methods.

2 MATERIAL POINT METHOD

MPM was developed to model fluid dynamics by Harlow et al. (1964) and later extended to history-dependent materials by Sulsky et al. (1994). The MPM-based approach describes the domain as a continuum media through a set of Lagrangian MPs that can move with the material through a computational mesh that covers the initial domain of the material and the expected domain invaded during calculation. Each MP represents a portion of the material domain and carries all the material information while the governing equations are solved at the nodes of the computational mesh, which is deformed based on the calculated updated velocities. Subsequently, the particle data is updated and the deformation mesh is reset to its original state. This double discretization allows the combination of positive features of the Eulerian and Lagrangian approaches and makes the method reliable for solving the governing equations under the hypothesis of small strains and for modelling large deformation problems in history-dependent materials.

Several formulations have been developed in MPM to address different conditions of saturation and drainage. The single-point formulation (where each MP represents a portion of the porous media) can be used to model one, two, or three phases (soil, liquid, and gas). In this study, the saturated soil is modeled under fully drained conditions, and, for simplicity, the analysis is performed using a single-point, one-phase formulation with the submerged unit weight, without calculating the pore water pressure.

2.1 *Contact formulation*

In standard MPM, the governing equations of different bodies are solved on the same background grid using a single-valued velocity field. Under this assumption, the contact interaction between bodies is automatically enforced, not allowing slip or separation at the contact. As a result, the method inherently produces a fully sticking contact behavior, which may not be representative of many physical problems involving frictional contact (Sulsky et al. 1994). An extended discussion on modelling contact formulations in MPM is given by Bird (2024) in the Introduction section.

Two main difficulties arise when dealing with non-stick frictional contact in MPM: (i) detecting contact; and (ii) computing the corresponding contact forces to prevent interpenetration and satisfy the frictional contact conditions.

Contact detection in MPM is not straightforward due to the possible nonconformity between the body domain and the background mesh, which makes it necessary to assess contact nodes at each time step of calculation. One of the most commonly used methods to detect contact is to identify interacting bodies when physical quantities, such as velocity or momentum, are mapped into the same background grid node.

This detection methodology was introduced in the pioneering work of Bardenhagen et al. (2000) to relax the non-slip condition between two bodies in contact. This procedure consists on a velocity prediction-correction scheme of nodal velocities. If two MPs from different bodies share the same node and are approaching each other, a correction to the normal component of the velocity is applied to prevent interpenetration, while a correction on the tangential component is introduced to satisfy the Mohr-Coulomb friction law. This velocity correction is equivalent to applying normal and tangential forces at the identified contact nodes.

Since the contact formulation proposed by Bardenhagen does not include contact forces in the momentum balance equations, the step in the MPM computational algorithm at which the predicted velocities must be corrected needs to be carefully evaluated for different MPM integration schemes. This issue is closely related to the treatment of Dirichlet boundary conditions, which are handled in a manner similar to the velocity prediction–correction step, and is discussed in detail by Buzzi et al. (2008).

The formulation proposed by Bardenhagen et al. (2000, 2001) was implemented within an Update Stress First (USF) MPM algorithm. In this framework, the velocity is corrected at two distinct steps: 1) when momentum balance is solved; and 2) when velocity is updated at MPs after computing the rate of momentum from nodal forces.

In the case of the Modified Updated Stress Last (MUSL) MPM integration scheme, Martinelli et al. (2020) and Galavi and Martinelli (2024), using a previous version of Anura3D, reported oscillations and non-conformity with contact constraints when applying the Bardenhagen contact formulation. To overcome these issues, the same authors adopted a hybrid approach in which an Updated Stress Last (USL) scheme is applied at contact nodes, while MUSL is maintained in the remainder of the domain. As a result, contact performance was improved. However, the drawbacks associated with the USL scheme, described by Sulsky et al. (1995), may still arise, including the so-called "low-mass" problem, which leads to unrealistically high numerical accelerations when MP are located close to one side of an element.

In this article, the MUSL integration scheme is applied throughout the entire domain. However, unlike the previously mentioned works, the correction of contact velocities is performed twice within the MPM computational algorithm, as described in detail in the following section. As a result, stress oscillations are reduced with respect to previous versions of the code, and the non-penetration condition is successfully enforced.

2.2 *Contact application in a MUSL integration scheme*

In the following, the contact algorithm implemented into a MUSL integration scheme is described (Figure 1):

STEP 1: Transfer MP masses and forces to the grid. If the contact formulation is applied, assemble the mass matrix separately for each body (subscript *b*).

$$\boldsymbol{M}_{b,i}^{t} = \sum_{el=1}^{N_{el,i}} \sum_{MP=1}^{N_{MP,el,b}} \boldsymbol{N}_i(\xi_{MP}^{t}) m_{MP} \tag{1}$$

$$\boldsymbol{f}_{b,i}^{int,t} = \sum_{el=1}^{N_{el,i}} \sum_{MP=1}^{N_{MP,el,b}} \boldsymbol{B}_i^{T}(\xi_{MP}^{t})\, \boldsymbol{\sigma}\, \Omega_{MP} \tag{2}$$

$$\boldsymbol{f}_{b,i}^{ext,t} = \sum_{el=1}^{N_{el,i}} \sum_{MP=1}^{N_{MP,el,b}} \boldsymbol{N}_i(\xi_{MP}^{t}) \boldsymbol{t}_{MP} + \sum_{el=1}^{N_{el,i}} \sum_{MP=1}^{N_{MP,el}} \boldsymbol{N}_i(\xi_{MP}^{t}) m_{MP}\, \boldsymbol{g} \tag{3}$$

where m_{MP} is the MP mass corresponding to the body *b*, $\xi_{\mathrm{MP}}^{\mathrm{t}}$ the MP local position at time *t*, $\mathbf{N}_{\mathrm{i}}$ the element shape function associated with node *i*, $\mathbf{B}_{\mathrm{i}}$ the shape function derivatives matrix, and $\mathbf{M}_{b,\mathrm{i}}^{\mathrm{t}}$ the lumped, diagonal mass matrix associated with node *i* for each body *b*. The vectors $\mathbf{f}_{\mathrm{i}}^{\mathrm{int,t}}$ and $\mathbf{f}_{\mathrm{i}}^{\mathrm{ext,t}}$ correspond to internal and external forces, respectively, at time *t* for node *i*.

$\mathbf{t}_{MP}$ denotes traction force vector, $\mathbf{g}$ the gravity vector, $\boldsymbol{\sigma}$ the stress tensor, and Ω_{MP} the MP volume.

STEP 2: Solve momentum balance at nodes for each body and for the system.

$$\mathbf{M}^{t}_{b,i}\,\mathbf{a}^{t}_{b,i} = \mathbf{f}^{ext,t}_{b,i} - \mathbf{f}^{int,t}_{b,i} \tag{4}$$

$$\mathbf{M}^{t}_{i}\,\mathbf{a}^{t}_{i} = \left(\sum_{b=1}^{N_b} \mathbf{M}^{t}_{b,i}\right)\mathbf{a}^{t}_{i} = \mathbf{f}^{ext,t}_{i} - \mathbf{f}^{int,t}_{i} \tag{5}$$

where $\mathbf{a}^{t}_{i}$ denotes the acceleration of the system and $\mathbf{a}^{t}_{b,i}$ the acceleration of each body *b*.

STEP 3: Body and system velocities are updated using the previously computed acceleration values.

$$\mathbf{v}^{t+\Delta t}_{b,i} = \mathbf{v}^{t}_{b,i} + \Delta t\,\mathbf{a}^{t}_{b,i} \tag{6}$$

$$\mathbf{v}^{t+\Delta t}_{i} = \mathbf{v}^{t}_{i} + \Delta t\,\mathbf{a}^{t}_{i} \tag{7}$$

The time increment is denoted by Δt.

STEP4: Apply essential BC and contact formulation.
Approaching condition is checked, being $\mathbf{n}_i$ the outward normal to contact body.

$$\left(\mathbf{v}^{t+\Delta t}_{b,i} - \mathbf{v}^{t+\Delta t}_{i}\right)\cdot\mathbf{n}_i > 0 \tag{8}$$

If Equation (8) is satisfied, a correction is applied to the normal component of the body velocities to enforce non-penetration according to Equation (10), and to the tangential component to satisfy the Mohr–Coulomb frictional contact condition in Equation (11). This results in the corrected velocity, denoted as $\tilde{\mathbf{v}}^{t+\Delta t}_{b,i}$.

$$\tilde{\mathbf{v}}^{t+\Delta t}_{b,i} = \mathbf{v}^{t+\Delta t}_{b,i} + \mathbf{c}^{t+\Delta t}_{norm,i} + \mathbf{c}^{t+\Delta t}_{tan,i} \tag{9}$$

$$\mathbf{c}^{t+\Delta t}_{norm,i} = -\left[\left(\mathbf{v}^{t+\Delta t}_{b,i} - \mathbf{v}^{t+\Delta t}_{i}\right)\cdot\mathbf{n}_i\right]\cdot\mathbf{n}_i \tag{10}$$

$$\mathbf{c}^{t+\Delta t}_{tan,i} = -\mu'\left[\left(\mathbf{v}^{t+\Delta t}_{b,i} - \mathbf{v}^{t+\Delta t}_{i}\right)\cdot\mathbf{n}_i\right](\mathbf{n}_i \times \hat{\boldsymbol{\omega}}) \tag{11}$$

where

$$\mu' = \min\left(\mu, \frac{\left|\left(\mathbf{v}^{t+\Delta t}_{b,i} - \mathbf{v}^{t+\Delta t}_{i}\right)\times\mathbf{n}_i\right|}{\left(\mathbf{v}^{t+\Delta t}_{b,i} - \mathbf{v}^{t+\Delta t}_{i}\right)\cdot\mathbf{n}_i}\right) \tag{12}$$

$$\hat{\boldsymbol{\omega}} = \frac{\left(\mathbf{v}^{t+\Delta t}_{b,i} - \mathbf{v}^{t+\Delta t}_{i}\right)\times\mathbf{n}_i}{\left|\left(\mathbf{v}^{t+\Delta t}_{b,i} - \mathbf{v}^{t+\Delta t}_{i}\right)\times\mathbf{n}_i\right|} \tag{13}$$

The normal velocity correction imposed in Equation (10) is equivalent to applying a force to the contact body to ensure that its normal velocity matches the system's normal velocity and, consequently, enforcing non-penetration. Tangential velocity correction in Equation (11) is equivalent to apply a tangential force to prevent relative tangential motion, when the magnitude of the tangential force is below the maximum sticking force. If the tangential force exceeds maximum sticking force, the frictional force is proportional to the magnitude of the normal force, with the proportionality coefficient μ'. These two alternative cases are achieved by defining a frictional coefficient μ' in Equation (12).

After correcting velocity for each body, a new corrected acceleration ($\tilde{\mathbf{a}}^{t+1}_{b,i}$) is computed.

$$\tilde{\mathbf{a}}^{t+1}_{b,i} = \left.\left(\tilde{\mathbf{v}}^{t+\Delta t}_{b,i} - \mathbf{v}^{t}_{b,i}\right)\right/\Delta t \tag{14}$$

STEP5: Update particle velocity with nodal acceleration.

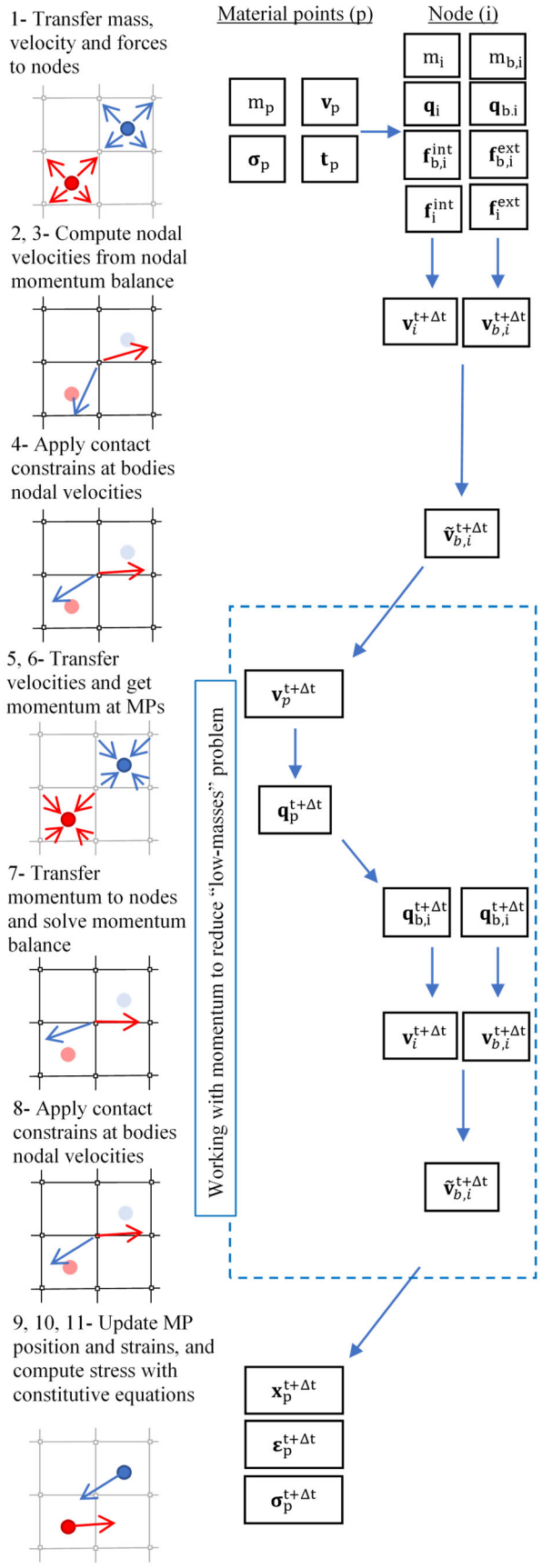

Figure 1: MPM MUSL flowchart.

$$\mathbf{v}_p^{t+1} = \mathbf{v}_p^t + \Delta t \sum_{i=1}^{N_n} \mathbf{N}_i(\xi_{MP}^t)\tilde{\mathbf{a}}_{b,i}^{t+1} \quad (14)$$

STEP6: Compute and transfer MP momentum to nodes.

$$\mathbf{q}_i^{t+1} = \sum_{el=1}^{N_{el,i}} \sum_{p=1}^{N_p} m_p \mathbf{N}_i(\xi_{MP}^t)\mathbf{v}_p^{t+1} \quad (15)$$

$$\mathbf{q}_{b,i}^{t+1} = \sum_{el=1}^{N_{el,i}} \sum_{p=1}^{N_{p,b}} m_p \mathbf{N}_i(\xi_{MP}^t)\mathbf{v}_p^{t+1} \quad (16)$$

STEP7: Update nodal velocities for system and bodies.

$$\mathbf{v}_i^{t+1} = \mathbf{q}_i^{t+1} / \mathbf{M}_i^t \quad (17)$$

$$\mathbf{v}_{b,i}^{t+1} = \mathbf{q}_{b,i}^{t+1} / \mathbf{M}_{b,i}^t \quad (18)$$

STEP8: Apply essential boundary conditions and the contact formulation, as in STEP4. Note that the same notation is used for both the corrected velocity and corrected acceleration.

STEP9: Update MP velocity and position from nodal values depending on the belonging body.

$$\boldsymbol{v}_p^{t+1} = \boldsymbol{v}_p^t + \Delta t \sum_{i=1}^{N_n} \boldsymbol{N}_i(\xi_{MP}^t)\tilde{\boldsymbol{a}}_{b,i}^{t+1} \quad (19)$$

$$\Delta \boldsymbol{u}_p^{t+1} = \Delta t\, \boldsymbol{v}_{b,i}^{t+1} \quad (20)$$

STEP10: Obtain MP strain increment from nodal values depending on the belonging body.

$$\Delta\boldsymbol{\varepsilon}_p^{t+1} = \left(\sum_{i=1}^{N_n} \mathbf{B}_i^T(\xi_{MP}^t)\mathbf{v}_{b,i}^{t+1}\right)\Delta t \quad (21)$$

STEP11: Update MP stresses.

$$\Delta\boldsymbol{\sigma}_p^{t+1} = \boldsymbol{D}\Delta\boldsymbol{\varepsilon}_p^{t+1} \quad (22)$$

$$\boldsymbol{\sigma}_p^{t+1} = \boldsymbol{\sigma}_p^t + \Delta\boldsymbol{\sigma}_p^{t+1} \quad (23)$$

Applying the contact formulation within the MUSL algorithm without performing the contact correction at STEP9 compromises the proper enforcement of contact constraints, leading to violations of the non-penetration condition. The proposed algorithm mitigates the low-mass problem associated with the USL scheme by solving the nodal momentum balance equation using the momentum rate from material points at STEP7, while allowing the MUSL scheme to be applied consistently throughout the entire model. The computational cost is not significantly affected in the case of the one-phase formulation considered (dry or drained saturated conditions).

3 NUMERICAL SIMULATION OF PIPE SOIL INTERACTION PROBLEM

3.1 *Centrifuge testing*

A set of centrifuge experiments described by Zhang et al. (1999, 2002) where carried out in the University of Western Australia centrifuge facility at 50g to understand unburied pipe-soil interaction with granular calcareous materials. The sand layer inside the centrifuge strongbox is 650 mm long and 140 mm high, while the modelled pipeline has a diameter of 20 mm. At prototype scale, this corresponds to a pipe diameter of 1 m, a sand layer length of 32.5 m, and a thickness of 7 m. Seabed calcareous sand from the North West Shelf of Australia was used. It is identified as a silty-sand (S-M) by comparing the granulometric curve after removing the 1% coarser particles with other studies using the same material (Mohr et al., 2013). After in-flight consolidation the unit weight of the soil was 18.1 kN/m^3 to 18.7 kN/m^3 with a void ratio in range 0.85 to 0.9.

The study presented in this paper focuses on one of the centrifuge tests, namely the probe test, which consists of two main phases: (i) an initialization phase, in which a monotonic vertical load is applied to achieve a prescribed embedment; and (ii) a second phase, in which the vertical load is maintained while a horizontal displacement is imposed and the resulting horizontal force is monitored.

The results show an increase in horizontal resistance force with increasing horizontal displacement (Figure 2). This behavior can be explained by two mechanisms: (i) an increase in the mobilized soil mass due to berm formation in the direction of movement; and (ii) an increase in embedment with horizontal displacement (Zhang et al., 1999).

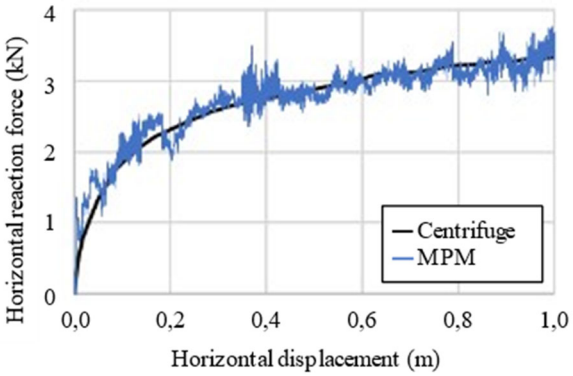

Figure 2: Horizontal force results from centrifuge test data and MPM.

3.2 *MPM modelling*

MPM model is carried out at centrifuge test scale (Figure 3). An unstructured triangular element mesh is used, with higher element density in the vicinity of the contact surface.

To apply the boundary conditions, a strongbox is included in the model. An additional layer of material with the same properties as the sand is placed between the boundary of the strongbox and the sand, characterized by a homogeneous local damping coefficient of 0.1 to reduce numerical oscillations.

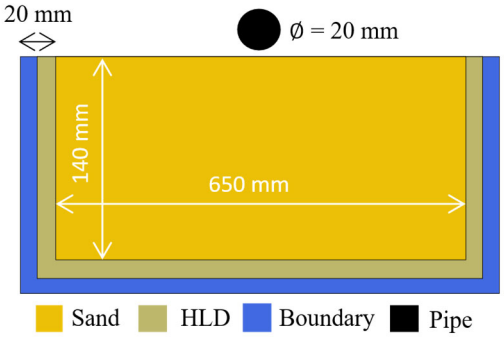

Figure 3: MPM model dimensions and initial geometry.

The calcareous sand is modeled as a drained saturated material (one-phase) using a Mohr-Coulomb constitutive model. Since Zhang et al. (1999, 2002) do not provide mechanical properties, it has been necessary to estimate the constitutive parameters.

The friction angle (35º) has been calibrated with monotonic penetration tests model (Zhang et al. 1999). No cohesion is expected for this type of sandy material (Lehane et al. 2014). An elastic modulus of 7 MPa was used in the calculations. A sensitivity analysis, not presented here, indicates that variations in this parameter do not have a relevant effect on the computed reaction forces. A Poisson's coefficient equal to 0.25 has been considered. Due to the large difference in stiffness between the soil and the structure, the pipe is considered completely rigid. The pipe–soil contact is modeled using a Mohr-Coulomb friction law, with a friction angle equal to two-thirds of the sand's friction angle and zero adhesion.

3.3 *Small strains FEM method*

Reaction to pipe horizontal displacement supposing a given initial embedment will be assessed with a small strain FEM "wished-in-place" analysis (WIP). A horizontal soil surface is considered because remolding of the material with initial penetration is not considered (Figure 4).

Two cases will be studied with the WIP method: supposing the initial embedment at the beginning of the probe test (0.1ϕ) and the final embedment at the end of the probe test (0.25ϕ).

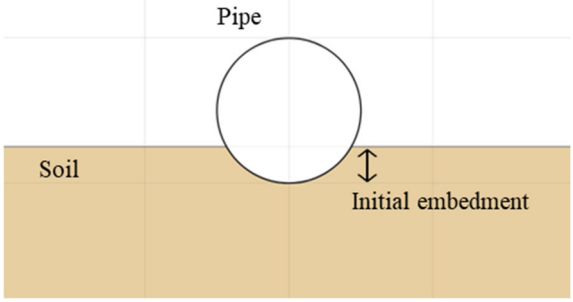

Figure 4: Small strains FEM initial geometry.

3.4 *Result comparison*

MPM results from the initial monotonic penetration phase showed good agreement with the experimental data. In the probe test, a vertical force of 4 kN was applied, which, according to the monotonic penetration test, corresponds to an initial embedment of 0.1Ø. The rapid increase in the contact surface due to the heaving of material at the sides of the embedded pipe was accurately captured by the MPM model.

In the second phase, the horizontal reaction force developed under the prescribed displacement shows good agreement with the experimental results (Figure 2). As reported by Zhang et al. (1999), the embedment of the tube increases with horizontal displacement, generating additional embedment that contributes to the rise in horizontal reaction force. Embedment grows rapidly with displacement and, after a horizontal displacement of approximately 0.3Ø, embedment reaches a maximum value of 0.25Ø. The accumulation of material in the berm formed in the direction of movement can explain the increase of horizontal force after arriving to the maximum embedment value.

To assess the capability of the FEM WIP analysis, two cases were evaluated: one corresponding to the initial embedment (0.1Ø) and another to the final embedment (0.25Ø). In both cases, the horizontal reaction force was underpredicted, reaching approximately 1 kN and 2 kN, respectively. For the initial embedment case, this underestimation can be attributed to FEM's inability to capture the increase in embedment and berm formation. In the second case, where the final embedment observed in the probe test was imposed as the input geometry, the results still did not match the experimental data. Although the maximum embedment from the centrifuge test was considered, the model fails to account for the accumulated material due to lateral displacement, which plays a significant role in the failure mechanism.

When comparing the failure mechanisms predicted by FEM WIP and MPM, both at the final embedment of 0.25Ø, two distinct geometries are observed. In FEM WIP (Figure), a two-wedge failure mechanism develops, whereas in MPM (Figure), failure appears to occur through the dragging of all mobilized material accumulated in the direction of displacement.

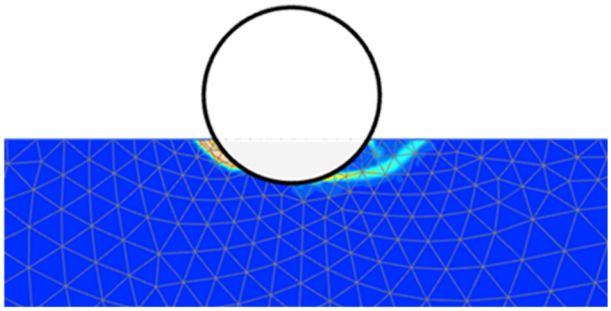

Figure 5: FEM WIP incremental deviatoric strains for a 0.25Ø embedment.

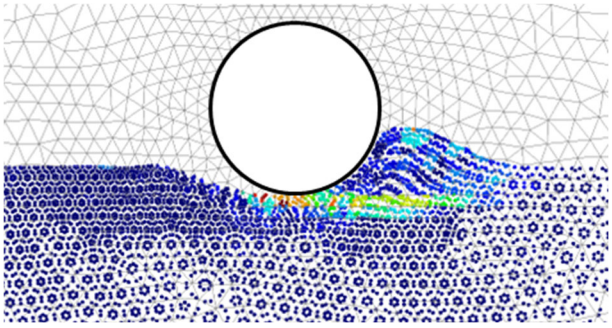

Figure 6: MPM incremental deviatoric strain for a 0.25Ø embedment and 0.3Ø horizontal displacement.

4 CONCLUSIONS

This paper demonstrates the capabilities of the Material Point Method (MPM) to model offshore unburied cable/pipe–soil interaction through the simulation of a centrifuge experiment. The contact formulation, a key aspect of the problem, is addressed by implementing a velocity predictor–corrector scheme (Bardenhagen et al., 2000) within a Modified Updated Stress Last (MUSL) MPM algorithm. A significant reduction in stress oscillations was observed compared to previous versions of the code.

MPM results are validated against centrifuge test data for calcareous sand. The probe test was modeled, and the force–displacement curve shows good agreement with the centrifuge measurements. Although images of soil deformation were not available for direct validation, failure mechanisms commonly reported in the literature were observed in the simulations. Once lateral displacement of the pipe begins after the initial embedment, the lateral soil reaction increases due to the accumulation of mobilized material around the pipe in the direction of movement, as well as the growth of embedment. Furthermore, a change in the failure mechanism is observed when the pipe reaches the maximum embedment (0.25Ø), transitioning from a clearly defined two-wedge mechanism to one resembling the dragging of mobilized material in the direction of movement.

Results from the centrifuge test and MPM simulations are compared with those obtained using a FEM "wished-in-place" (WIP) model, a method commonly used in industry for this type of problem. The FEM WIP model underestimates the soil's horizontal reaction to displacement due to its inability to

account for mobilized material and the increase in embedment. Even when the final embedment is prescribed in the FEM WIP model, the horizontal reaction remains underpredicted. These results indicate that the FEM WIP approach is not suitable for this type of problem, whereas MPM provides a more accurate and reliable solution.

5 ACKNOWLEDGEMENTS

The first author acknowledges the support of Secretariat for Universities and Research of the Generalitat de Catalunya. through the Joan Oró grant (ref. BDNS 657443). The second author thanks the financial support received from the Serra Húnter Program put forward by the Department of Enterprise and Knowledge of the Secretariat for Universities and Research of the Generalitat de Catalunya. The authors acknowledge the financial support of the project PDC2022-133222-I00 and PID2022-141429OB-I00 funded by MCIN/AEI/10.13039/501100011033/FEDER and Union Europea NextGenerationEU/PRTR. The authors also acknowledge the support of Anura3D MPM Research Community.

6 REFERENCES

Anura3D MPM Research Community (2025) Anura3D Version 2025 Source Code. https://www.anura3d.com

Bardenhagen, S., Brackbill, J.U., Sulsky, D. (2000). The material-point method for granular materials. Computer Methods in Applied Mechanics and Engineering, Volume 187, Issues 3–4, Pages 529-541, ISSN 0045-7825. https://doi.org/10.1016/S0045-7825(99)00338-2

Bardenhagen, S., Guilkey, J., Roessig, K., Brackbill, J., Witzel, W., Foster, J. (2001). An improved contact algorithm for the material point method and application to stress propagation in granular material. CMES. Computer Modeling in Engineering & Sciences. 2. 10.3970/cmes.2001.002.509. https://doi.org/10.3970/cmes.2001.002.509

Buzzi, O., Pedroso, D., Giacomini, A. (2008). Caveats on the implementation of the generalized material point method. Computer Modeling in Engineering and Sciences. 31. https://doi.org/10.3970/cmes.2008.031.085

Bird, R., Pretti, G., Coombs, W., Augarde, C., Sharif, Y., Brown, M., Carter, G., Macdonald, C., Johnson, K. (2024). An implicit material point-to-rigid body contact approach for large deformation soil-structure interaction. Computers and Geotechnics. 174. 106646. 10.1016/j.compgeo.2024.106646.

Chatterjee, S., Randolph, M. F., & White, D. J. (2012). The effects of penetration rate and strain softening on the vertical penetration resistance of seabed pipelines. Géotechnique, 62(7), 573-582. https://doi.org/10.1680/geot.10.P.075

Di Carluccio, G., Pinyol, N., Alonso, E., Hürlimann, M. (2023). Liquefaction-induced flow-like landslides: the case of Valarties (Spain). Géotechnique. 74. 307-324. 10.1680/jgeot.21.00112.

Dingle, H. R. C., White, D. J., & Gaudin, C. (2008). Mechanisms of pipe embedment and lateral breakout on soft clay. Canadian Geotechnical Journal, 45(5), 636-652. https://doi.org/10.1139/T08-009

European commission. (2020a). Communication from the Commission to the European Parliament, the Council, the European Economic and Social Committee and the Committee of the Regions: Stepping up Europe's 2030 climate ambition. Investing in a climate-neutral future for the benefit of our people. (COM/2020/176 final)

European commission. (2020b). Offshore renewable energy. (https://energy.ec.europa.eu/topics/renewable-energy/offshore-renewable-energy_en)

Galavi, V. & Martinelli, M. (2024). MPM Simulation of the Installation of an Impact-Driven Pile in Dry Sand and Subsequent Axial Bearing Capacity. Journal of Geotechnical and Geoenvironmental Engineering. 150. 10.1061/JGGEFK.GTENG-11592.

Ghosh, S., Kikuchi, N. (1991) An arbitrary Lagrangian-Eulerian finite element method for large deformation analysis of elastic-viscoplastic solids. Computer Methods in Applied Mechanics an Engineering, Volume 86, Issue 2, Pages 127-188, ISSN 0045-7825, https://doi.org/10.1016/0045-7825(91)90126-Q.

Gourvenec, S. & Randolph, M. F. (2011). Offshore Geotechnical Engineering. 10.1201/9781315272474.

Hu, Y., Randolph, M. F. (1998). A practical numerical approach for large deformation problems in soil. International Journal of Numerical and Analytical Methods in Geomechanics, 22 (5), pp. 327-350. https://doi.org/10.1002/(SICI)1096-9853(199805)22:5<327: AID-NAG920>3.0.CO;2-X

Lehane, B. M., H. Carraro, J. A., Boukpeti, N., & Elkhatib, S. (2014). Mechanical Response of Two Carbonate Sediments from Australia's North West Shelf. Volume 3: Offshore Geotechnics, V003T10A008. https://doi.org/10.1115/OMAE2014-23340

Martinelli, M., E. Alderlieste, D. Luger, and V. Galavi. (2020). Numerical simulation of the installation of suction buckets using MPM. Proc., 4th Int. Symp. on Frontiers in Offshore Geotechnics (ISFOG 2020 in 2022). Hawthorne, NJ: Deep Foundations Institute

Merifield, R., White, D. J., & Randolph, M. F. (2008). The ultimate undrained resistance of partially embedded pipelines. Géotechnique, 58(6), 461-470. https://doi.org/10.1680/geot.2008.58.6.461

Mohr, Henning & Draper, Scott & White, David. (2013). Free Field Sediment Mobility on Australia's North West Shelf. Proceedings of the International Conference on Offshore Mechanics and Arctic Engineering - OMAE. 4. 10.1115/OMAE2013-11490.

Murff, J. D., Wagner, D. A. & Randolph, M. F. (1989). Pipe penetration in a cohesive soil. Géotechnique Vol 39 Issue 2, June 1989, pp. 213-229. https://doi.org/10.1680/geot.1989.39.2.213

Randolph, M. F., & White, D. J. (2008b). Upper-bound yield envelopes for pipelines at shallow embedment in clay. Géotechnique, 58(4), 297-301. https://doi.org/10.1680/geot.2008.58.4.297

Sulsky, D., Chen, Z., and Schreyer, H. L. (1994) A Particle Method for History-Dependent Materials, Comput. Meths. Appl. Mech. Engrg. 118: 179-196. https://doi.org/10.1016/0045-7825(94)90112-0.

Sulsky, D., Zhou, S., Schreyer, H. (1995). Application of particle-in-cell method to solid mechanics. Computer Physics Communications. 87. 236-252. 10.1016/0010-4655(94)00170-7.

Wang, D., White, D. J., & Randolph, M. F. (2010). Large-deformation finite element analysis of pipe penetration and large-amplitude lateral displacement. Canadian Geotechnical Journal, 47(8), 842-856. https://doi.org/10.1139/T09-147

Westgate, Z. J., White, D. J., & Randolph, M. F. (2009). Video Observations of Dynamic Embedment During Pipelaying in Soft Clay. Volume 3: Pipeline and Riser Technology, 699-707. https://doi.org/10.1115/OMAE2009-79814

Zhang, J., Randolph, M., & Stewart, D. P. (1999). An Elasto-Plastic Model for Pipe-Soil Interaction of Unburied Pipelines. In J. S. Chung, T. Matsui, & W. Koterayama (Eds.), The Proceedings of the Ninth (1999) International Offshore and Polar Engineering Conference (Brest, France ed., Vol. 2, pp. 185-192). International Society of Offshore and Polar Engineers.

Zhang, J., Stewart, D. P., & Randolph, M. F. (2002). Modeling of Shallowly Embedded Offshore Pipelines in Calcareous Sand. Journal of Geotechnical and Geoenvironmental Engineering, 128(5), 363-371. https://doi.org/10.1061/(ASCE)1090-0241(2002)128:5(363)

Zambrano, Luis & Yerro, Alba. (2020). Numerical simulation of a free fall penetrometer deployment using the material point method. Soils and Foundations. Tokyo. 60. 10.1016/j.sandf.202